**Climate
of the Past**
Discussions

Orbital forcing of terrestrial hydrology, weathering and carbon sequestration during the Palaeocene-Eocene Thermal Maximum

Tom Dunkley Jones[1]*, Hayley R. Manners[2,3], Murray Hoggett[1], Sandra Kirtland Turner[4], Thomas
Westerhold[5], Melanie J. Leng[6], Richard D. Pancost[7], Andy Ridgwell[4], Laia Alegret[8], Rob Duller[9],
Stephen T. Grimes[2]

[1] School of Geography, Earth and Environmental Sciences, University of Birmingham, Edgbaston, Birmingham, B15 2TT,
UK.
[2] School of Geography, Earth & Environmental Sciences, Plymouth University, Drake Circus, Plymouth, Devon, PL4 8AA,
UK.
[3] School of Ocean and Earth Sciences, National Oceanography Centre, University of Southampton, Southampton, SO14
3ZH, UK.
[4] Department of Earth Sciences, University of California, Riverside, CA 92521, USA
[5] MARUM — Center for Marine Environmental Sciences, University of Bremen, Leobener Strasse, 28359 Bremen,
Germany.
[6] NERC Isotope Geosciences Facilities, British Geological Survey, Nottingham NG12 5GG, UK & Centre for Environmental
Geochemistry, University of Nottingham, Nottingham, NG7 2RD, UK.
[7] Organic Geochemistry Unit, The Cabot Institute, School of Chemistry, University of Bristol, Bristol, BS8 1TS, UK.
[8] Departamento de Ciencias de la Tierra & Instituto Universitario de Ciencias Ambientales, Universidad de Zaragoza, 50009
Zaragoza, Spain.
[9] Department of Earth, Ocean and Ecological Sciences, University of Liverpool, Liverpool, L69 3GP

Correspondence to: Tom Dunkley Jones (t.dunkleyjones@bham.ac.uk)

Abstract. The response of the Earth System to greenhouse-gas driven warming is of critical importance
for the future trajectory of our planetary environment. Hypethermal events - past climate transients with
significant global-scale warming - can provide insights into the nature and magnitude of these
responses. The largest hyperthermal of the Cenozoic was the Palaeocene-Eocene Thermal Maximum
(PETM ~56 Ma). Here we present a new high-resolution cyclostratigraphy for the classic PETM section
at Zumaia, Spain. With this new age model we are able to demonstrate that detrital sediment
accumulation rates within this continental margin section increased more than four-fold during the
PETM, representing a radical change in regional hydrology that drove dramatic increases in terrestrial
to marine sediment flux. During the body of the PETM, orbital-scale variations in bulk sediment Si/Fe
ratios are evidence for the continued orbital pacing of sediment erosion and transport processes, most
likely linked to precession controls on sub-tropical hydroclimates. Most remarkable is that detrital
accumulation rates remain high throughout the body of the PETM, and even reach peak values during
the recovery phase of the characteristic PETM carbon isotope excursion (CIE). Using a series of Earth
System Model inversions, we demonstrate that the silicate weathering feedback alone is insufficient to
recover the PETM CIE, and that active organic carbon burial is required to match the observed
dynamics of the CIE. Further, that the period of maximum organic carbon sequestration coincides with
the peak in detrital accumulation rates observed at Zumaia. Based on these results, we hypothesize that

precession controls on tropical and sub-tropical hydroclimates, and the sediment dynamics associated with this variation, play a significant role in the timing of the rapid climate and CIE recovery from peak-PETM conditions.

1 Introduction

5 The PETM is a marked interval of climate warming (Dunkley Jones et al., 2013), shoaling of oceanic carbonate saturation horizons (Zachos et al., 2005) and a large global negative Carbon Isotope Excursion (CIE) in all rapidly exchangeable marine and terrestrial carbon reservoirs (McInerney and Wing, 2011). The most consistent explanation for these coupled perturbations is the release of carbon from a large shallow lithospheric reservoir, with a depleted carbon isotopic (δ^{13}C) signature (~ –20 to –

10 60 ‰), on a multi-millenial timescale (Bowen et al., 2015; Dickens et al., 1995; Gutjahr et al., 2017b; Kirtland Turner and Ridgwell, 2016; Zeebe et al., 2016). Although there is still no confidence on the identity of such a large (>4000 Pg C) and unstable carbon reservoir, its release and oxidation within the ocean-atmosphere system caused rising atmospheric CO_2 concentrations, warming and a range of Earth System perturbations associated with pronounced global warming (Sluijs et al., 2007).

15
Although considerable attention has been paid to constraining the rates of carbon release, based on deep-ocean carbonate dissolution (Panchuk et al., 2008; Zachos et al., 2005; Zeebe et al., 2009), rates of warming (Meissner et al., 2014; Zeebe et al., 2016), carbon isotope profiles (Bowen et al., 2015; Kirtland Turner and Ridgwell, 2016) and surface ocean pH (Gutjahr et al., 2017a) the mechanisms

20 responsible for both the climatic and isotope recovery at the end of this transient event are still not well constrained (Bowen and Zachos, 2010). The timescales of silicate weathering and carbonate burial (~100-200 ka) are suggested to be too long to drive the main phase of CIE recovery, which the best records available to date indicate is an order of magnitude faster (~10-20 ka) (Bowen and Zachos, 2010). However, observed patterns of enhanced carbonate and possibly biogenic silica deposition in the

25 deep-ocean through the PETM recovery phase are interpreted as the signature of a silicate weathering-driven recovery (Penman, 2016; Penman et al., 2016). The alternative mechanism for carbon removal is the substantial burial of organic carbon within either terrestrial or marine sedimentary systems (Bowen and Zachos, 2010). One means of increasing global organic carbon burial rates is through enhanced sedimentation rates on continental margins, which might contribute significantly to C_{org} burial rates

30 with little or no rise in measured total weight percent organic carbon content of sediments (Sluijs et al., 2014). There is also direct evidence for substantial increases in the organic carbon content of syn-PETM marine sediments in the eastern Tethys, associated with increased terrestrial to marine weathering fluxes and reduced seawater oxygenation (Carmichael et al., 2017; Gavrilov et al., 1997).

35 If organic carbon burial does drive recovery from the PETM, there is no explanation for the temporal offset between increased sedimentation rates and organic carbon burial during the body of the PETM (John et al., 2008) – when models indicate no or little carbon removal from the systems – and the major phase of carbon burial required for the CIE recovery at the end of the event. Models that include a continued leakage of carbon to maintain a prolonged CIE provide a mechanism to delay recovery

(Penman et al., 2016; Zeebe et al., 2009), but this delay only exacerbates the mismatch between the observed fast recovery and the timescales of silicate weathering-driven carbon drawdown (Penman et al., 2016). As yet, there is no satisfactory model to explain the timing of the large-scale carbon drawdown required to drive the rapid CIE recovery phase ~100 ka after the onset of the PETM (Bowen

5 and Zachos, 2010). Understanding the ultimate fate of thousands of petagrams of "excess" carbon injected into the ocean-atmosphere system during the PETM has profound implications for understanding the behaviour of the Earth's climate future over the coming millennia. Here, we present new sedimentological records from the Iberian upper continental slope (~1000m paleo-water depth), constrained within a detailed new cyclostratigraphic age model to address the linkage between climatic

10 controls on sedimentation rates and carbon drawdown.

2 The Zumaia PETM succession

2.1 Cyclostratigraphy

Our studied PETM section is located at the Itzurun beach-front of the town of Zumaia, northern Spain (Figure 1; N 043°18´4.5", W 002°15´31.2"). Situated within the deep-basin of the Pyrenean Gulf, it is

15 the deep-water end of a sediment distribution system that has been mapped in detail over the past two decades (see references and summary within Pujalte et al., 2015). Logged sections span terrestrial alluvial fans and plains, shallow shelf carbonates, incised channel distribution systems and a deep-water basin (Pujalte et al., 2015 and references therein). Within this, the Zumaia section is regarded as the most complete and representative end member of the deep-water depositional system, recording the

20 distal deposition of fluvial-derived fine grained sediment plumes (Pujalte et al., 2015) at middle-lower bathyal (1000 m) paleodepths (Alegret et al., 2009). The aim of this study is to build on the existing detailed depositional framework developed for the region, and to use the Zumaia section as a key recorder of the temporal patterns of climate-driven sediment flux from terrestrial systems to the deep ocean during the PETM.

25

Although the Zumaia section is a classic PETM locality and the subject of a series of bio-, magneto-, chemo-, and lithostratigraphic studies (Alegret et al., 2009; Baceta et al., 2000; Bernaola et al., 2007; Canudo et al., 1995; Dinarès-Turell et al., 2007; Manners et al., 2013; Schmitz et al., 1997; Schmitz et al., 2001; Storme et al., 2012), there is, as yet, no robust cyclostratigraphic framework established for

30 the distinct 'fine-grained siliciclastic unit' (FSU), which spans the majority of the PETM CIE (Figure 2). To generate a cyclostratigraphic framework, we took a total of 248 small "thumbnail" 1cc bulk sediment samples at ~3 to 5cm resolution from ~4.3 m below to ~8.2 m above the onset of the characteristic "siliciclastic unit" that marks the body of the PETM at this location. The zero reference point for all sampling is taken at the top of the prominent limestone bed, located ~0.3 m below the base

35 of the SU. In between the limestone and the SU is a 0.3 m thick greenish-grey marl unit, which is distinct from both the limestone / marl units found above and below the SU and the typically red-brown clays and marly clays of the SU itself. The section was logged in detail, and integrated with the existing stratigraphic framework for the site (Figure 2).

Climate
of the Past

Discussions

All samples were analysed for bulk sediment elemental composition by X-ray Fluoresence (XRF) using dried, powered sediment, mounted in wax pellets. Pellets were analysed with a Bruker S8 tiger X-Ray
5   Fluorescence (XRF) Spectrometer with 8-minute analysis time, at the University of Birmingham (UoB). CaO concentrations from XRF analyses were converted into high-resolution estimates of weight percent $CaCO_3$ using a calibration set of 25 discrete calcium carbonate measurements. Weight percent $CaCO_3$ contents were determined at UoB, based on inorganic carbon contents measured by CO_2 generation with phosphoric acid reaction within a 200ºC furnace using a Shimadzu TOC-V carbon analyser. Detrital
10   MARs were estimated assuming that both detrital and carbonate fractions had an estimated dry bulk density of 1.8 g cm^{-3}. Organic carbon MARs were calculated following (2009).

A subset of 129 thumbnail samples were also analysed for the stable isotope composition ($\delta^{13}C_{carb}$ and $\delta^{18}O_{carb}$) of bulk carbonates at the NERC Isotope Geosciences Laboratory (NIGL, Keyworth,
15   Nottingham). Sample material was powdered to yield CO_2 from the equivalent of 10 mg of 100% calcite and reacted with anhydrous phosphoric acid *in vacuo* overnight at a constant 25°C. Liberated CO_2 was separated from water vapour under vacuum and collected for analysis. Measurements were made on a VG Optima mass spectrometer (standard reproducibility of $< \pm 0.1$‰). All data are on the VPDB scale. An additional 67 bulk samples were analysed for total organic carbon content at NIGL
20   using a Carlo Erba 1500 elemental analyser with acetanilide used as the calibration standard. Replicate analyses indicated a precision of ± 0.1 wt% in well-mixed samples (1 Standard Deviation, SD).

New analyses resolve a prominent cyclicity in SiO_2 and Si/Fe ratios both below and above the SU (Figure 2), corresponding to the established precession-paced lithological cycles in this setting (Dinarès-
25   Turell et al., 2003; Westerhold et al., 2008). Through the SU itself, 10 Si/Fe cycles are identified between the CIE onset and the $\delta^{13}C$ inflection point F of Röhl et al. (2007; Figure 2). With a total CIE duration of 90-167 ka (Murphy et al., 2010; Röhl et al., 2007) these are most likely half-precession cycles (10*10.5=105 ka) of a similar nature to those in terrestrial palaeosol successions from the Bighorn Basin. These are likely linked to catchment hydrology (e.g. Abdul Aziz et al., 2008), resulting
30   from the interference of both northern and southern hemisphere precession signals within tropical hydroclimates (Short et al., 1991). This is consistent with a strong hydroclimate control on sediment erosion and transport in the Tremp-Graus terrestrial basins during the PETM (Pujalte et al., 2015; Schmitz and Pujalte, 2007).

35   Above the SU, two prominent thicker carbonate beds are correlated with the 100 ka eccentricity minima of Westerhold *et al.* (Westerhold et al., 2007; precession cycles 6/7 and 11), which is supported by the placement of the Last Rare Occurrence of the calcareous nannofossil genus *Fasciculithus* at 8.7 m (Baceta et al., 2006; confirmed by Dunkley Jones, pers. obs.), between cycles 15 and 16, which is consistent with Forada section and ODP Site 690 (Röhl et al., 2007). Significant power is resolved at
40   frequencies of ~2.2 cycles m^{-1} (~0.45 m period) and 0.7 cycles m^{-1} (~1.4 m period) (Figure 3), which are taken to be half-precession and precession cycles respectively. This double peak in power spectra is unlikely to be due to a simple step-change in sedimentation rates at the onset of the PETM conditions –

with an associated shift in the frequency of precession signals in the depth domain - as power is resolved at both frequencies within the body of the PETM where sedimentation rates are relatively stable (Figure 2). Based on the resolution of these ten cycles within the siliciclastic unit, we have managed to extend the existing cyclostratigraphy for the Zumaia section through the body of the PETM,

5   developing a detailed age model and calculated sedimentation rates (Figure 4).

2.2 The Zumaia Carbon Isotope Excursion (CIE)

Prior to the onset of the CIE at Zumaia, benthic foraminifera extinctions begin in the greenish-grey marl unit between the top of a characteristic limestone band (0 m) and the onset of the PETM (0.3 m) (Alegret et al., 2009). The main phase of benthic foraminifera extinctions is precisely coupled with the

10 onset of the CIE at 0.3 m (Alegret et al., 2009). The CIE onset is rapid with a ~3.3 ‰ negative shift between 0.3 and 0.38 m (~0 to 4.7 ka after onset) with a further decline to values of ~ -4.0 ‰ or lower above 0.5 m (~12 ka after onset; total CIE of more than ~3.7 ‰; Figure 2). Although the doubling of sedimentation rates at the onset of the PETM limits the effects of any carbonate burndown on the $\delta^{13}C_{carb}$ record across the onset, $\delta^{13}C_{carb}$ data appear to diverge from the typical PETM CIE profile

15 between ~0.7 to 2.8m. Here, $\delta^{13}C_{carb}$ values return to higher values, of ~ –3‰, which lie between those of the peak CIE and pre-excursion values (Figure 2). This is attributed to the increased relative contribution of reworked detrital carbonates, as evidenced by the presence of Cretaceous nannofossils (Dunkley Jones, pers. obs.), during periods of very low autochthonous carbonate flux. This is supported by the return of $\delta^{13}C_{carb}$ to near peak-excursion values once carbonate contents increase above 2.8m.

20 Above this level, there is a CIE recovery phase similar to other high-resolution records from the deep ocean (e.g. Zachos et al., 2005; Figure 5).

The new age model for Zumaia enables a direct comparison to both existing deep ocean (Rohl et al., 2007) and terrestrial (Bowen et al., 2014) locations that have a comparable cyclostratigraphic

25 framework (Figure 5). In the rate of CIE onset – defined as time to peak negative CIE values - and the magnitude of the CIE excursion, the Zumaia $\delta^{13}C$ record is clearly more similar to the Big Horn Basin soil carbonate $\delta^{13}C$ record than to other deep-ocean sites (Figure 5). In both sections the main CIE onset is marked by a ~4‰ negative $\delta^{13}C$ shift, with a duration of between ~2 and 12 ka. This excursion value is then maintained for ~80 ka, during a relatively stable "plateau" phase (~55.93 to 55.85 Ma), before a

30 relatively quick main recovery phase, which is slightly quicker at Zumaia (~55.85 to 55.82 Ma) than in the Bighorn Basin (55.85 to 55.81 Ma). In the deep ocean, sedimentary records of the PETM onset are typically condensed due to extensive carbonate dissolution (Bralower et al., 2014). Combined with sediment mixing, this tends to smooth $\delta^{13}C_{carb}$ profiles, reducing the apparent rate of onset of the event, whilst maintaining an appearance of stratigraphic continuity (Bralower et al., 2014; Kirtland Turner and

35 Ridgwell, 2016). The greatly increased flux of fine-grained detrital sediment from nearby terrestrial basins (Pujalte et al., 2015) into the Zumaia section creates an expanded rather than condensed PETM onset with far greater stratigraphic and temporal fidelity. Once plotted on a common age model the dissolution-controlled lag in time to peak CIE conditions in the deep-ocean bulk $\delta^{13}C$ is clearly visible, and of the order of 70 ka even in the shallowest and most complete sections (ODP Sites 690 & 1263;

peak CIE ~55.86 Ma; Figure 5). Once peak values are reached, the deep-ocean sites show a similar quick CIE recovery phase to Zumaia between 55.85 and 55.82 Ma.

2.3 Calcium Carbonate and Detrital Sediment Mass Accumulation Rates

Based on the cyclostratigraphic age model and estimated weight % $CaCO_3$, we estimate calcium
5   carbonate, total organic carbon (TOC) and detrital mass accumulation rates (MAR) throughout the study interval (Figures 4 and 5). Carbonate MAR closely follows weight % $CaCO_3$, with a marked decline during the body of the SU. The records do, however, diverge in two key intervals: first during the distinct limestone bed below the onset of the PETM, between ~ -0.8 and 0 m (~56.03 to 55.95 Ma), and then in the later stage of the CIE recovery between ~4.4 and 4.7m (55.82 to 55.81 Ma) (Figures 4
10   and 5). In the first of these, the distinct high carbonate content of the limestone unit is weakly represented in carbonate MAR, indicating that this is the result of clastic sediment starvation, rather than increased carbonate production. The second horizon occurs during the CIE recovery phase, when carbonate MARs nearly treble compared to pre-PETM values before stabilizing at levels ~50% higher than pre-PETM conditions during the post-PETM phase above 4.7 m (~55.81 Ma). This persistent
15   increase in carbonate MARs above the PETM is reflected in consistently higher carbonate contents ($CaCO_3$ wt %) of sediments above the PETM than those in the latest Paleocene. This is clear evidence for significantly increased carbonate accumulation rates post-PETM, even in relatively shallow (~1000m) supra-lysoclinal depths on the continental margins. The rate and timing of this recovery in carbonate MARs is also remarkable, with not only recovery to background levels, but also this switch to
20   significantly elevated MARs all occurring within the main phase of the CIE recovery in less than 20 ka (Figure 5).

The mass accumulation rate of non-carbonate components is here considered equal to the detrital MAR, in the absence of any significant contribution of biogenic silica. Before the CIE, the detrital MARs are
25   relatively low, fluctuating around 2 g cm^{-2} ka^{-1}, with a further decline during the precursor limestone unit (–0.8 to 0 m). During the onset of the PETM (0.3 – 1.5 m) detrital fluxes increase dramatically, to between three and four times pre-PETM levels. Within the peak-PETM (1.5-1.7 m; ~55.88 to 55.85 Ma), detrital flux declines slightly and shows variability on similar timescales to Si/Fe ratios. It then increases markedly towards the end of the peak-PETM interval, above 3.7 m (~55.85 Ma), and reaches
30   peak values for the whole PETM during the main phase of the $\delta^{13}C$ recovery interval (3.7 – 4.2 m; ~55.83 to 55.82 Ma). Both detrital and carbonate MAR increase, to peak values for the whole PETM, during the main interval of CIE recovery, with detrital MARs peaking first, followed by carbonate MARs. We note that these high detrital mass accumulations rates during the body of the PETM do not coincide with a noticeable increase in grain size, with sediments dominated by clay-grade material
35   throughout. This is consistent with the marked absence of coarser grained turbidite deposition during the PETM within the Zumaia section (Clare et al., 2015), although major increases in coarse grained siliciclastic deposits during the PETM are recorded within deep-water channels within the basin (Pujalte et al., 2015). Total organic carbon MARs are relatively stable before the onset of the event, at ~0.01 g cm^{-2} ka^{-1}. At the onset of the PETM there is an increase in TOC MARs, but this lags the CIE onset by
40   ~20 ka (Figure 5). During the body of the PETM there are distinct peaks in TOC MARs at ~55.90 Ma

Climate
of the Past
Discussions

and ~55.85 Ma, but in general values remain between 0.015 and 0.02 g cm^{-2} ka^{-1}. Coincident with recovery the CIE recovery phase, TOC MARs increase again to over ~0.02 g cm^{-2} ka^{-1} between 55.83 and 55.81 Ma.

3 Inverse Modelling the Zumaia CIE and the PETM carbon source

5   To constrain the rates of carbon input and sequestration through the onset and termination of the PETM, based on the CIE profile and cyclostratigraphy from Zumaia, we undertook a series of PETM simulations using the late Palaeocene-early Eocene configuration of the cGENIE Earth System Model. This includes a 3-D dynamic ocean model, 2D energy balance atmospheric model, and a representation of marine biogeochemical cycling plus the preservation of carbonates in deep-sea sediments (Ridgwell

10   and Schmidt, 2010). We also include a 0-D (global average) temperature-dependent terrestrial weathering feedback as described in (Colbourn et al., 2013). We follow a two-part spin-up procedure, first for 20 ka as a 'closed' system (i.e. weathering exactly balancing sedimentation) and with atmospheric CO_2 set to 834 ppm with a $\delta^{13}C$ of -4.9‰. A further 250 ka 'open system' spin-up with temperature-dependent weathering feedbacks enabled and input of CO_2 via volcanic outgassing

15   (Colbourn et al., 2013) was used to bring the geological ^{13}C cycle to steady state. In this, the specified detrital flux to the sediments (non-carbonate) (0.18 g cm^{-2} ka^{-1}), the rain ratio of carbonate to particulate organic carbon (0.2), and the global average concentrations of Mg^{2+} and Ca^{2+} (29.89 and 18.22 mmol kg^{-1}, respectively) and alkalinity (1975 µmol kg^{-1}) were selected to give an average global mean sedimentary carbonate preservation of 46.75%, comparable with late Paleocene estimates (Panchuk et

20   al., 2008).

Four inversion experiments were undertaken, all forced with carbon (CO_2) inputs to the atmosphere such that the $\delta^{13}C$ of surface ocean dissolved inorganic carbon (DIC) followed a prescribed inversion target taken from the Zumaia $\delta^{13}C$ record, adjusted to the initial cGENIE average surface ocean DIC

25   $\delta^{13}C$ of +2.7‰. Within the very low carbonate interval, where the primary signals appear to be lost due to the disproportionate influence of non-autochthonous carbonates, the $\delta^{13}C$ target curve was linearly interpolated between the data points at ~19 and 78 ka. Experiments included variation in the isotope composition of the source (–60‰ and –22‰) and CIE recovery driven by silicate weathering only and with active carbon removal to match the CIE profile (Table 1). In order to directly compare modelled

30   and observed carbonate contents, all experiments also include the temporally varying observed changes in detrital fluxes within the sediment model at the model grid-box corresponding to the paleolocation of Zumaia only.

Net input fluxes depend on the $\delta^{13}C$ composition of the source (Table 1), with smaller carbon inputs

35   required for a source with a more negative isotope composition. Total carbon inputs are also slightly larger where no removal fluxes are allowed (Experiment 1). In all experiments, the majority of C input occurs in the first 20 ka with a low rate of C input (<0.05 Pg C yr-1) required to maintain low isotope values until 78 ka. Total modelled C input is broadly comparable to previous model-based estimates constrained by deep-ocean carbonate dissolution that exceed ~4000 Pg C (Bowen et al., 2015; Cui et al.,

2011; Gutjahr et al., 2017a; Panchuk et al., 2008). In this case the lower bound of carbon input (4154 PgC) is generated by an inversion of the CIE isotopic profile assuming a pure biogenic methane carbon source with isotope composition of –60‰. As an independent test of the reliability of these simulations, in terms of the estimated CIE magnitude and temporal dynamics, the modelled atmospheric $\delta^{13}C$

5   excursion is compared to the best available terrestrial record of the CIE, from soil carbonates of the Bighorn Basin (Figure 6; Bowen et al., 2014). There is a strong correspondence between the two, in the shape of the onset and recovery, the magnitude of the CIE and the overall duration of the event. Although these model runs have no independent second constraint on the carbon cycle perturbation through the PETM – for example a measure of surface ocean pH change (Gutjahr et al., 2017c) or deep

10   ocean carbonate saturation state (Panchuk et al., 2008; Zeebe et al., 2009) – model simulations with a mixed source input with $\delta^{13}C$ of -22 ‰ are close in total mass input across the PETM onset (11,316 Pg C) to the preferred simulations of Gutjahr et al. (2017; ~10,200 Pg C), which are constrained by surface ocean pH changes. The combination of these two records – pH from DSDP Site 401 and the CIE dynamics from Zumaia – is, however, informative. Total carbon input masses, constrained by the most

15   detailed surface ocean pH records of the PETM available to date, are modelled to be >10,000 Pg C (Gutjahr et al., 2017c), but the dynamics of this release must be considerably quicker than assumed within the deep-ocean records recovered from Site DSDP Site 401, in order to satisfy the rate of CIE onset observed at Zumaia, which is ~3.3 ‰ over less than 5 ka. We argue that this CIE onset rate is robust, given that it is observed in both terrestrial (Bowen et al., 2015) and marine (this study) sections

20   where the onset of the CIE is expanded and set within a robust intra-PETM cyclostratigraphic age model. The CIE recorded at Zumaia, and within the Big Horn Basin (Bowen et al., 2015), of 4 ‰ or more, is also greater than that assumed in the favoured model simulations of Gutjahr et al. (2017) of 2.6 ‰, and is closer to their alternate run assuming a CIE of ~4 ‰, which reconstructs a source carbon source with a $\delta^{13}C$ composition of ~ -17 ‰. Both these aspects of the Zumaia record – a CIE onset less

25   than 5 ka, and a CIE with magnitude ~4 ‰ or more – requires the rapid release of carbon from a source that is more isotopically-depleted than volcanic CO_2. Whether thermogenic methane generated by sill intrusion during the onset phase of the NAIP (Svensen et al., 2004) can meet the emission rates and carbon isotopic compositions required to generate the early stages of the CIE is yet to be resolved.

4 Carbon Removal During the PETM Recovery

30   Two fundamental unknowns remain about the recovery phase of the PETM: first, what is the ultimate sink of thousands of petagrams of carbon when added to the ocean-atmopshere system as CO_2?; and, second, what controls the temporal dynamics of carbon flux into this sink, and thence controls the timing of the relatively rapid CIE and PETM climate recovery? The combination of the age-constrained CIE records from Zumaia, the inverse Earth System modelling of this CIE and the general excellent

35   agreement between the atmospheric CIE generated in these simulations with independent records from the terrestrial realm (Figure 6; Bowen et al., 2015), provide new insights into these key questions. In simulations without active carbon removal, the only process restoring atmospheric pCO_2 to pre-CIE levels is the silicate weathering feedback, where net removal depends on the size of the carbon input and associated temperature change. This "weathering only" experiment fails to match the observed CIE

recovery, with minimal recovery of atmospheric CO_2 $\delta^{13}C$ even when a significant mass of carbon has been removed from the atmosphere (Figure 6). This is due to the isotopic imbalance between the ultimate carbon sink in this case – marine carbonates (-1 to 4‰) – compared to the carbon source (–22 or –60 ‰). With the weathering feedback only, the rate of removal of carbon from the atmosphere

5   (Figure 6), and associated climate recovery, also occurs on timescales significantly longer (> 100 ka) than indicated by climate proxy data, where temperatures are closely coupled to the recovery of the CIE (Dunkley Jones et al., 2013). The configuration of the silicate weathering feedback within the model is thus an insufficient driver of PETM recovery on two counts: first its inability to drive recovery in the carbon isotopic composition of the exogenic carbon reservoir, and second, in its inability to match the

10 rate of recovery of the climate system at the end of the PETM. The Zumaia record also provides evidence for a rapid climate transition at the end of the PETM, independent of carbon-cycle system parameters (e.g. $\delta^{13}C$ and $CaCO_3$ accumulation), in the observed rapid switch back to pre-PETM detrital fluxes during the recovery phase. This implies a rapid climate recovery - back to a hydrological and erosive system similar to pre-event conditions - that is very closely coupled to the CIE recovery (Figure

15 5).

To correctly simulate both the CIE and the climate system (temperature, hydrology) recovery rates, the active removal of large masses of isotopically light carbon is required during the PETM recovery phase. Simple isotope mass balance requirements require a greater mass of carbon to be removed than was first

20 released, if the isotopic composition of the sink is more positive (organic carbon -22 %) than that of the source (biogenic methane -60 %). In these methane input / organic carbon burial simulations (Experiment 4), the required excess carbon removal (removal mass minus input mass) causes a remnant post-event climate forcing, with an ~60% decline in post-PETM atmospheric CO_2 levels relative to pre-PETM conditions (Figure 6), and a global mean surface temperature reduction of ~ 4ºC. At present

25 there is no evidence for such a post-PETM cooling, which would suggest that the source and sink terms are relatively close in their isotopic compositions and precludes a biogenic methane input / organic carbon burial scenario.

The simulations that best match the constraints of the CIE and PETM recovery are those with the active

30 removal of carbon, focused on the main phase of the CIE recovery, and with an isotopic composition close to that of the original carbon source. The failure of the silicate weathering feedback alone to match the rate and magnitude of CIE recovery is similar to the recent inverse modelling by Gutjahr et al. (2017), where 2,500 Pg of carbon removal, with isotopic composition of -30.5 ‰, was required to match the CIE. The larger masses of carbon removal required in the simulations presented here are due

35 to the smaller magnitude CIE recorded at DSDP Site 401, the target CIE curve for Gutjahr et al. (2017), and the isotopically lighter composition of the carbon sink used (-30.5 ‰) by Gutjahr et al. (2017) compared to this study (-22 ‰).

The question remains as to what is the driver of enhanced carbon burial during the CIE recovery

40 interval? In the Zumaia records it is notable that exactly this interval – the CIE recovery phase – is directly coupled with maxima in total sedimentation rates and detrital mass accumulation rates (Figure 5). There is also a close coupling between these peak detrital fluxes and a transient peak in carbonate

9

MAR, which is exactly the coupling predicted if increased detrital accumulation is accompanied by the widespread burial of organic carbon, with a resultant rapid increase in ocean pH and carbonate saturation state (Bowen and Zachos, 2010). Inverse Earth System modelling of the CIE at this location demonstrates that this interval of peak MARs (~80 to 120 ka after onset) is coincident with ~8700 Pg of

5   carbon drawdown from the ocean-atmosphere system in the -22 ‰ δ^{13}C input and removal scenario, equivalent to ~87 % of total removal fluxes. The magnitude of increase in detrital accumulation rates at the end of the event (from <6 to >8 g cm^{-2} ka^{-1}) is also of the same order as the ~40% increase in organic carbon burial rates estimated for the CIE recovery (Bowen and Zachos, 2010). Although Zumaia is a single PETM record from a single location, it has striking similarities to other Tethyan

10   deep-water successions, such as Forada in Italy (Giusberti et al., 2016), and is likely representative of regional-scale dynamics of climate and the associated response of continental margin sedimentary systems. Within the main phase of the PETM, variability within the Forada section is interpreted to be precession-paced wet and arid phases associated with a monsoonal-type subtropical climate (Giusberti et al., 2016). Measured TOC MARs through the Zumaia section are elevated during the recovery

15   interval, ~55.83 to 55.81 Ma (Figure 5), although these data are not able to discriminate between the burial fluxes of old (pre-PETM) reworked carbon and those for newly produced (intra-PETM) organic carbon – only the later will contribute to the removal of carbon from the exogenic carbon cycle. The Zumaia records cannot yet be used to trace the rates of burial of new-formed organic carbon through the PETM recovery phase, however they do provide a feasible mechanism for the timing of the recovery

20   phase of the PETM, namely a strong precession-forcing of tropical and sub-tropical hydrological regimes and associated sediment erosion, flux and accumulation. Alongside the observed precession-forced variations in sediment accumulation, there is likely a complex influence of temperature and CO_2 on the balance between rates of net primary production and organic carbon remineralization during the PETM (Cotton et al., 2015). This production / remineralization balance will control the availability of

25   newly formed sedimentary organic carbon for long-term burial in the sedimentary carbon sink (Cotton et al., 2015). During conditions of peak PETM warmth, enhanced organic carbon remineralization in terrestrial systems may have drastically limited the flux to continental margin systems, but with even a gradual recovery from peak-warmth conditions – forced, for example, by known enhanced carbon burial in the anoxic marine basins of the eastern Tethys during the peak-PETM (Carmichael et al., 2017) - a

30   subtle shift in the production to respiration balance towards the availability of organic carbon for long-term burial, combined with a precession-forced peak in sediment flux and accumulation rates across terrestrial and continental margin systems, could account for the magnitude and timing of the sudden switch to widespread carbon sequestration required during the CIE recovery phase. The greatly enhanced detrital accumulation rates observed in continental margin settings such as Zumaia could also

35   effectively mask patterns of enhanced burial of newly formed organic matter (Sluijs et al., 2014), unless sedimentation rates within the PETM can be accurately constrained. Future studies should also focus on discriminating the relative contributions of newly formed (intra-PETM) and reworked "fossil" (pre-PETM) organic carbon within these continental margin successions, as only the former will contribute to carbon sequestration.

Climate
of the Past
Discussions

5 Conclusions

New high-resolution bulk sediment chemistry records across the PETM interval of the Zumaia section allow, for the first time, the extension of the well-established precession-based cyclostratigraphy through the characteristic low carbonate siliciclastic unit that marks peak-PETM conditions. Ten intra-
5   PETM cycles in bulk sediment Si/Fe ratios are consistent with the newly established cyclostratigraphic framework for the Big Horn Basin and its correlation to classic PETM deep-ocean sites (Westerhold et al., 2017). This new cyclostratigraphic framework for Zumaia, together with new bulk carbonate isotopic data and Earth System modelling of the Zumaia PETM CIE, constrains some key components of the PETM event:

10   • CIE onset rates and magnitude recorded at Zumaia are in close agreement with soil carbonate nodule data from the Big Horn Basin, and imply PETM onset times of less than 5000 years, with a CIE magnitude of at least ~4 ‰.
   • During the deposition of the characteristic PETM siliciclastic unit of Zumaia, sedimentation rates double and the mass accumulation rates of detrital sediments increase by up to four times relative to
15   pre-event conditions.
   • Dramatic increases in sedimentation rates during the main phase of the PETM are interpreted to represent significant changes in regional hydrology, most likely an increase in the magnitude and frequency of extreme rainfall and runoff events, potentially within an overall lower mean annual precipitation regime (Carmichael et al., 2017; Carmichael et al., 2016). These changes in sedimentation
20   accumulation rates – and inferred perturbations to hydrology - persist throughout the PETM interval, only returning towards pre-event levels during the rapid phase of CIE recovery. This supports a close coupling between the CIE and the climate system.
   • During the PETM bulk sediment composition and flux vary on timescales consistent with a component of precession forcing of regional subtropical hydroclimates. This infers a significant role for
25   orbital-paced insolation variability in pacing global climate throughout the extreme climate state of the PETM.
   • Earth System Model (cGENIE) inversion experiments, designed to replicate the observed CIE dynamics at Zumaia, reproduce an atmospheric CIE that is close to the best available terrestrial records of the CIE (Bowen et al., 2015), in timing and magnitudes. Depending on the $\delta^{13}C$ composition of the
30   source of PETM carbon, estimated total carbon inputs during the onset of the PETM are ~3,400 Pg C (methane source, -60 ‰) or ~11,300 Pg C (organic carbon source, -22 ‰).
   • Simulations with a silicate weathering only feedback and mechanism for carbon cycle recovery fail to reproduce the observed record in two key ways: first, they are unable to recover the coupled CIE-climate system at a rate fast enough to match the observations (<20 ka); and, second, the final sink of
35   carbon within this feedback – marine carbonates – is isotopically too heavy to provide any significant recovery of the CIE.
   • Simulations that match the patterns of CIE recovery require active organic or methane carbon removal, of a magnitude similar to the original carbon input. Simulations with an isotopic mismatch between source carbon (methane -60 ‰) and sink carbon (organic matter -22 ‰) require significantly
40   more carbon removal at the end of the event than originally released during the onset. This causes a

11

marked post event cooling of ~4 ºC relative to pre-event conditions that is inconsistent with current climate records.

• Peak sedimentation rates and detrital accumulation rates are observed through the recovery phase of the CIE and not the onset. We suggest that this peak in sedimentation rates is coupled to the precession
5 forcing of subtropical terrestrial hydrology and that this intra-PETM variability provides a key to understanding the timing of the recovery phase of the CIE. A widespread, precession-forced peak in sediment flux within tropical to sub-tropical environments, potentially coupled to increased rainfall, runoff and sediment transport, provides a mechanism for increased organic carbon burial across a range of terrestrial and continental margin sediment sinks. If this is coupled with a gradual change in the
10 temperature / CO_2-controlled balance between net primary production to organic carbon remineralization rates (Cotton et al., 2015), such that organic carbon becomes more available for burial as temperatures begin to recover from peak-PETM conditions, this may have the potential to provide a rapid recovery feedback through a cycle of cooling and enhanced organic carbon burial.

15 The results presented here demonstrate that the Earth System was capable of the sequestration of several thousand petagrams of carbon at the end of the PETM, but only after nearly one hundred thousand years within a profoundly altered climate state. The mechanism of carbon burial also appears to rely on a radical perturbation to global hydroclimates, sufficient to cause erosion and dramatically increased sediment flux rates to continental margins between three and four times pre-perturbation levels.
20

ADDITIONAL INFORMATION
Supplementary information is available in the online version of the paper. Correspondence and requests for materials should be addressed to TDJ.

35 **References**

Abdul Aziz, H., Hilgen, F. J., Van Luijk, G. M., Sluijs, A., Kraus, M. J., Pares, J. M., and Gingerich, P. D., 2008, Astronomical climate control on paleosol stacking patterns in the upper Paleocene–lower Eocene Willwood Formation, Bighorn Basin, Wyoming: Geology, v. 36, no. 7, p. 531.

Alegret, L., Ortiz, S., Orue-Etxebarria, X., Bernaola, G., Baceta, J. I., Monechi, S., Apellaniz, E., and Pujalte, V., 2009, The Paleocene-Eocene Thermal Maximum: New data on microfossil turnover at the Zumaia section, Spain: Palaios, v. 24, no. 5, p. 318-328.

Baceta, J. I., Pujalte, V., and Caballero, F., 2006, Paleocene and Early Eocene Facies and Events: a

5   Basin-Platform-Coastal Plain Transect (South-Central and Western Pyrenees). Climate and Biota of the Early Paleogene 2006. Post Conference Field Trip Guidebook, Bilbao.

Baceta, J. I., Pujalte, V., Dinarès-Turell, J., Payros, A., Orue-Etxebarria, X., and Bernaola, G., 2000, The Paleocene/Eocene boundary interval in teh Zumaia Section (Gipuzkoa, Basque Basin): Magnetostratigraphy, and high-resolution lithostratigraphy: Revista de la Sociedad Geológica de

10   España, v. 13, p. 375-391.

Bernaola, G., Baceta, J. I., Orue-Etxebarria, X., Alegret, L., Martin-Rubio, M., Arostegui, J., and Dinares-Turell, J., 2007, Evidence of an abrupt environmental disruption during the mid-Paleocene biotic event (Zumaia section, western Pyrenees): Geological Society of America Bulletin, v. 119, no. 7-8, p. 785-795.

15   Bowen, G. J., Maibauer, B. J., Kraus, M. J., Röhl, U., Westerhold, T., Steimke, A., Gingerich, P. D., Wing, S. L., and Clyde, W., 2014, Two massive, rapid releases of carbon during the onset of the Palaeocene-Eocene thermal maximum: Nature Geoscience, v. 8, p. 44-47.

Bowen, G. J., Maibauer, B. J., Kraus, M. J., Rohl, U., Westerhold, T., Steimke, A., Gingerich, P. D., Wing, S. L., and Clyde, W. C., 2015, Two massive, rapid releases of carbon during le onset of the

20   Palaeocene-Eocene thermal maximum: Nature Geoscience, v. 8, no. 1, p. 44-47.

Bowen, G. J., and Zachos, J. C., 2010, Rapid carbon sequestration at the termination of the Palaeocene--Eocene Thermal Maximum: Nature Geoscience, v. 3, no. 12, p. 866-869.

Bralower, T. J., Kelly, D. C., Gibbs, S., Farley, K., Eccles, L., Lindemann, T. L., and Smith, G. J., 2014, Impact of dissolution on the sedimentary record of the Paleocene-Eocene thermal maximum: Earth and

25   Planetary Science Letters, v. 401, p. 70-82.

Canudo, J. I., Keller, G., Molina, E., and Oritz, N., 1995, Planktic foraminiferal turnover and d13C isotopes across the Paleocene-Eocene transition at Caravaca and Zumaya, Spain: Palaeogeography Palaeoclimatology Palaeoecology, v. 114, p. 75-100.

Carmichael, M. J., Inglis, G. N., Badger, M. P. S., Naafs, B. D. A., Behrooz, L., Remmelzwaal, S.,

30   Monteiro, F. M., Rohrssen, M., Farnsworth, A., Buss, H. L., Dickson, A. J., Valdes, P. J., Lunt, D. J., and Pancost, R. D., 2017, Hydrological and associated biogeochemical consequences of rapid global warming during the Paleocene-Eocene Thermal Maximum: Global and Planetary Change, v. 157, p. 114-138.

Carmichael, M. J., Lunt, D. J., Huber, M., Heinemann, M., Kiehl, J. T., LeGrande, A., Loptson, C. A.,

35   Roberts, C. D., Sagoo, N., Shields, C., Valdes, P. J., Winguth, A., Winguth, C., and Pancost, R. D., 2016, A model-model and data-model comparison for the early Eocene hydrological cycle: Climates of the Past, v. 12, p. 455-481.

Clare, M. A., Talling, P. J., and Hunt, J. E., 2015, Implications of reduced turbidity current and landslide activity for the Initial Eocene Thermal Maximum - evidence from two distal, deep-water sites:

40   Earth and Planetary Science Letters, v. 420, p. 102-115.

Colbourn, G., Ridgwell, A., and Lenton, T., 2013, The rock geochemical model (RokGeM) v0.9: Geoscientific Model Development, v. 6, no. 5, p. 1543-1573.

13

Cotton, J. M., Sheldon, N. D., Hren, M. T., and Gallagher, T. M., 2015, Positive feedback drives carbon release from soils to atmosphere during Paleocene/Eocene warming: American Journal of Science, v. 315, no. 4, p. 337-361.

Cui, Y., Kump, L. R., Ridgwell, A. J., Charles, A. J., Junium, C. K., Diefendorf, A. F., Freeman, K. H., Urban, N. M., and Harding, I. C., 2011, Slow release of fossil carbon during the Palaeocene--Eocene Thermal Maximum: Nature Geoscience, v. 4, no. 7, p. 481-485.

Dickens, G. R., O'Neil, J. R., Rea, D. K., and Owen, R. M., 1995, Dissociation of oceanic methane hydrate as a cause of the carbon isotope excursion at the end of the Paleocene: Paleoceanography, v. 10, no. 6, p. 965-971.

Dinarès-Turell, J., Baceta, J., Bernaola, G., Orue-Etxebarria, X., and Pujalte, V., 2007, Closing the Mid-Palaeocene gap: Toward a complete astronomically tuned Palaeocene Epoch and Selandian and Thanetian GSSPs at Zumaia (Basque Basin, W Pyrenees): Earth and planetary science letters, v. 262, no. 3-4, p. 450-467.

Dinarès-Turell, J., Baceta, J. I., Pujalte, V., Orue-Etxebarria, X., Bernaola, G., and Lorito, S., 2003, Untangling the Palaeocene climatic rhythm: an astronimically calibrated Early Palaeocene magnetostratigraphy and biostratigraphy at Zumaia (Basque basin, northern Spain): Earth and Planetary Science Letters, v. 216, p. 483-500.

Dunkley Jones, T., Lunt, D. J., Schmidt, D. N., Ridgwell, A., Sluijs, A., Valdes, P. J., and Maslin, M., 2013, Climate model and proxy data constraints on ocean warming across the Paleocene/Eocene Thermal Maximum: Earth-Science Reviews, v. 125, no. 0, p. 123-145.

Gavrilov, Y. O., Kodina, L., Lubchenko, I., and Muzylev, N., 1997, The late Paleocene anoxic event in epicontinental seas of the Peri-Tethys and formation of the sapropelite unit: Sedimentology and geochemistry: Lithology and Mineral Resources, v. 32, p. 427-450.

Giusberti, L., Galazzo, F. B., and Thomas, E., 2016, Variability in climate and productivity during the Paleocene-Eocene Thermal Maximum in the western Tethys (Forada section): Climate of the Past, v. 12, no. 2, p. 213-240.

Gutjahr, M., Ridgwell, A., Sexton, P. F., Anagnostou, E., Pearson, P. N., P‚àö¬ßlike, H., Norris, R. D., Thomas, E., and Foster, G. L., 2017a, Very large release of mostly volcanic carbon during the Palaeocene-Eocene Thermal Maximum: Nature, v. 548, p. 573-577.

Gutjahr, M., Ridgwell, A., Sexton, P. F., Anagnostou, E., Pearson, P. N., P√§like, H., Norris, R. D., Thomas, E., and Foster, G. L., 2017b, Very large release of mostly volcanic carbon during the Palaeocene-Eocene Thermal Maximum: Nature, v. 548, p. 573-577.

John, C. M., Bohaty, S. M., Zachos, J. C., Sluijs, A., Gibbs, S., Brinkhuis, H., and Bralower, T. J., 2008, North American continental margin records of the Paleocene-Eocene thermal maximum: Implications for global carbon and hydrological cycling: Paleoceanography, v. 23, p. doi:10.1029/2007PA001465.

Kirtland Turner, S., and Ridgwell, A., 2016, Development of a novel empirical framework for interpreting geological carbon isotope excursions, with implications for the rate of carbon injection across the PETM: Earth and Planetary Science Letters, v. 435, p. 1-13.

Manners, H. R., Grimes, S., Sutton, P. A., Domingo, L., Leng, M. J., Twitchett, R. T., Hart, M. B., Dunkley Jones, T., Pancost, R. D., Duller, R., and Lopez-Martinez, N., 2013, Magnitude and profile of organic carbon isotope records from the Palaeocene-Eocene Thermal Maximum: evidence from northern Spain: Earth and Planetary Science Letters, v. 377, p. 220-230.

14

McInerney, F. A., and Wing, S. L., 2011, The Paleocene-Eocene Thermal Maximum: A perturbation of carbon cycle, climate, and biosphere with implications for the future: Annual Review of Earth and Planetary Sciences.

Meissner, K. J., Bralower, T., Alexander, K., Dunkley Jones, T., Sijp, W., and Ward, M., 2014, The
5 Paleocene-Eocene Thermal Maximum: How much carbon is enough?: Paleoceanography, v. 29, p. 946-963.

Murphy, B. H., Farley, K. A., and Zachos, J. C., 2010, An extraterrestrial 3He-based timescale for the Paleocene-Eocene thermal maximum (PETM) from the Walvis Ridge, IODP Site 1266: Geochemica et Cosmochemica Acta, v. 74, p. 5098-5108.

10 Panchuk, K., Ridgwell, A., and Kump, L., 2008, Sedimentary response to Paleocene-Eocene Thermal Maximum carbon release: A model-data comparison: Geology, v. 36, no. 4, p. 315.

Penman, D. E., 2016, Silicate weathering and North Atlantic silica burial during the Paleocene-Eocene Thermal Maximum: Geology, v. 44, no. 9, p. 731-734.

Penman, D. E., Turner, S. K., Sexton, P. F., Norris, R. D., Dickson, A. J., Boulila, S., Ridgwell, A.,
15 Zeebe, R. E., Zachos, J. C., Cameron, A., Westerhold, T., and Rohl, U., 2016, An abyssal carbonate compensation depth overshoot in the aftermath of the Palaeocene-Eocene Thermal Maximum: Nature Geoscience, v. 9, no. 8, p. 575-+.

Pujalte, V., Baceta, J. I., and Schmitz, B., 2015, A massive input of coarse-grained siliciclastics in the Pyrenean Basin during the PETM: the missing ingredient in a coeval abrupt change in hydrological
20 regime: Climate of the Past, v. 11, no. 12, p. 1653-1672.

Ridgwell, A., and Schmidt, D. N., 2010, Past constraints on the vulnerability of marine calcifiers to massive carbon dioxide release: Nature Geoscience, v. 3, no. 3, p. 1-5.

Röhl, U., Westerhold, T., Bralower, T., and Zachos, J., 2007, On the duration of the Paleocene-Eocene thermal maximum (PETM): Geochemistry, Geophysics, Geosystems, v. 8, no. 12, p. 1-13.

25 Rohl, U., Westerhold, T., Bralower, T. J., and Zachos, J. C., 2007, On the duration of the Paleocene-Eocene thermal maximum (PETM): Geochemistry Geophysics Geosystems, v. 8.

Schmitz, B., Asaro, F., Molina, E., Monechi, S., Salis, K. v., and Speijer, R. P., 1997, High-resolution iridium, d13C, d18O, foraminifera and nannofossil profiles across the latest Paleocene benthic extinction event at Zumaya: Palaeogeography Palaeoclimatology Palaeoecology, v. 133, p. 49-68.

30 Schmitz, B., and Pujalte, V., 2007, Abrupt increase in seasonal extreme precipitation at the Paleocene-Eocene boundary: Geology, v. 35, no. 3, p. 215-218.

Schmitz, B., Pujalte, V., and Nunez-Betelu, K., 2001, Climate and sea-level perturbations during the Initial Eocene Thermal Maximum: evidence from siliciclastic units in the Basque Basin (Ermua, Zumaia and Trabakua Pass), northern Spain: Palaeogeography Palaeoclimatology Palaeoecology, v.
35 165, no. 3-4, p. 299-320.

Short, D. A., Mengel, J. G., Crowley, T. J., Hyde, W., and North, G. R., 1991, Filtering of Milankovitch Cycles by Earth's Geography: Quaternary Research, v. 35, p. 157-173.

Sluijs, A., Bowen, G. J., Brinkhuis, H., Lourens, L. J., and Thomas, E., 2007, The Palaeocene-Eocene Thermal Maximum super greenhouse: biotic and geochemical signatures, age models and mechanisms
40 of global change, *in* Williams, M., Haywood, A. M., Gregory, J., and Schmidt, D. N., eds., Deep-time perspectives on climate change: Marrying the signal from computer models and biological proxies: London, The Micropalaeontological Society Special Publication, p. 323-350.

Sluijs, A., van Roij, L., Harrington, G. J., Schouten, S., Sessa, J. A., Levay, L. J., Reichart, G. J., and Slomp, C. P., 2014, Warming, euxinia and sea level rise during the Paleocene-Eocene Thermal Maximum on the Gulf Coastal Plain: implications for ocean oxygenation and nutrient cycling: Climate of the Past, v. 10, no. 4, p. 1421-1439.

5   Storme, J.-Y., Devleeschouwer, X., Schnyder, J., Cambier, G., Baceta, J. I., Pujalte, V., Di Matteo, A., Iacumin, P., and Yans, J., 2012, The Palaeocene/Eocene boundary section at Zumaia (Basque-Cantabric Basin) revisited: new insights from high-resolution magnetic susceptibility and carbon isotope chemostratigraphy on organic matter (δ13Corg): Terra Nova, v. 00, p. 1-9.

Svensen, H., Planke, S., Malthe-Sorenssen, A., Jamtveit, B., Myklebust, R., Eidem, T., and Rey, S.,
10   2004, Release of methane from a volcanic basin as a mechanism for initial Eocene global warming: Nature, v. 429, no. 6991, p. 542-545.

Westerhold, T., Röhl, U., Laskar, J., Raffi, I., Bowles, J., Lourens, L., and Zachos, J., 2007, On the duration of magnetochrons C24r and C25n and the timing of early Eocene global warming events: Implications from the Ocean Drilling Program Leg 208 Walvis Ridge depth transect: Paleoceanography,
15   v. 22, no. 2.

Westerhold, T., Rohl, U., Raffi, I., Fornaciari, E., Monechi, S., Reale, V., Bowles, J., and Evans, H. F., 2008, Astronomical calibration of the Paleocene time: Palaeogeography Palaeoclimatology Palaeoecology, v. 257, no. 4, p. 377-403.

Westerhold, T., Röhl, U., Wilkens, R., Gingerich, P. D., Clyde, W., Wing, S., Bowen, B., and Kraus,
20   M., 2017, Synchronizing early Eocene deep-sea and continental records - new cyclostratigraphic age models from the Bighorn Basin Coring Project: Climates of the Past Discussions.

Willmott, V., Rampen, S., Domack, E., Canals, M., Sinninghe Damste, J. S., and Schouten, S., 2009, Holocene changes in *Proboscia* diatom productivity in shelf waters of the north-western Antarctic Peninsula: Antarctic Science, v. 22, no. 1, p. 3-10.

25   Zachos, J. C., Röhl, U., Schellenberg, S. A., Sluijs, A., Hodell, D. A., Kelly, D. C., Thomas, E., Nicolo, M., Raffi, I., Lourens, L. J., McCarren, H., and Kroon, D., 2005, Rapid acidification of the ocean during the Paleocene-Eocene thermal maximum: Science, v. 308, no. 5728, p. 1611-1615.

Zeebe, R. E., Ridgwell, A., and Zachos, J. C., 2016, Anthropogenic carbon release rate unprecedented during the past 66 million years: Nature Geoscience, v. 9, p. 325-329.

30   Zeebe, R. E., Zachos, J. C., and Dickens, G. R., 2009, Carbon dioxide forcing alone insufficient to explain Palaeocene-Eocene Thermal Maximum warming: Nature Geoscience, v. 2, no. 8, p. 576-580.

Table 1. Summary details of cGENIE simulations detailing isotopic compositions of source carbon - input during the onset of the PETM to match Zumaia CIE profile – and the nature of modelled CIE recovery, whether by silicate weathering only (Experiment 1), or by active carbon removal. The isotopic

5 composition of this carbon removal ("Sink") is also listed. Net C fluxes are calculated by the model to match the CIE profile and do not include carbon removed through silicate weathering.

Experiment	$\delta^{13}C$ composition		Net C flux (PgC)			Average Emission Rates (Pg C yr^{-1})	
	Source	Sink	0 to 19 ka	19 to 78 ka	>78 ka	0 to 19 ka	19 to 78 ka
1. Mixed source; silicate weathering	–22 ‰	Carbonate burial	+11376	+1809	0	0.60	0.03
2. Mixed source; terrestrial carbon burial	–22 ‰	–22 ‰ (C$_{org}$)	+11316	+1809	-10083	0.60	0.03
3. Methane source; methane removal	–60 ‰	–60 ‰ (CH$_4$)	+3382	+772	-3244	0.18	0.01
4. Methane source; terrestrial carbon burial	–60 ‰	–22 ‰ (C$_{org}$)	+3483	+2360	-8640	0.18	0.04

10
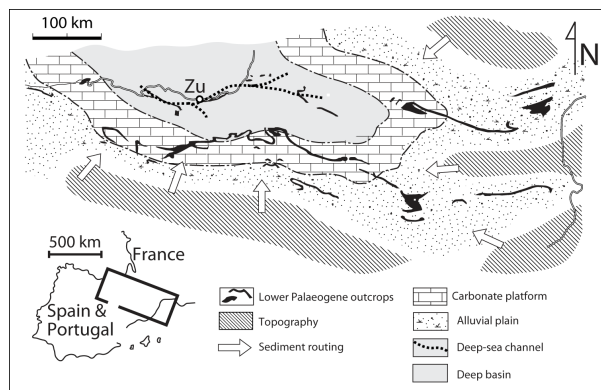
Figure 1: Location of Zumaia section and relationship to the terrestrial and shallow shelf carbonate depositional environments; after Pujalte et al. (2015).

15

Climate
of the Past

Discussions
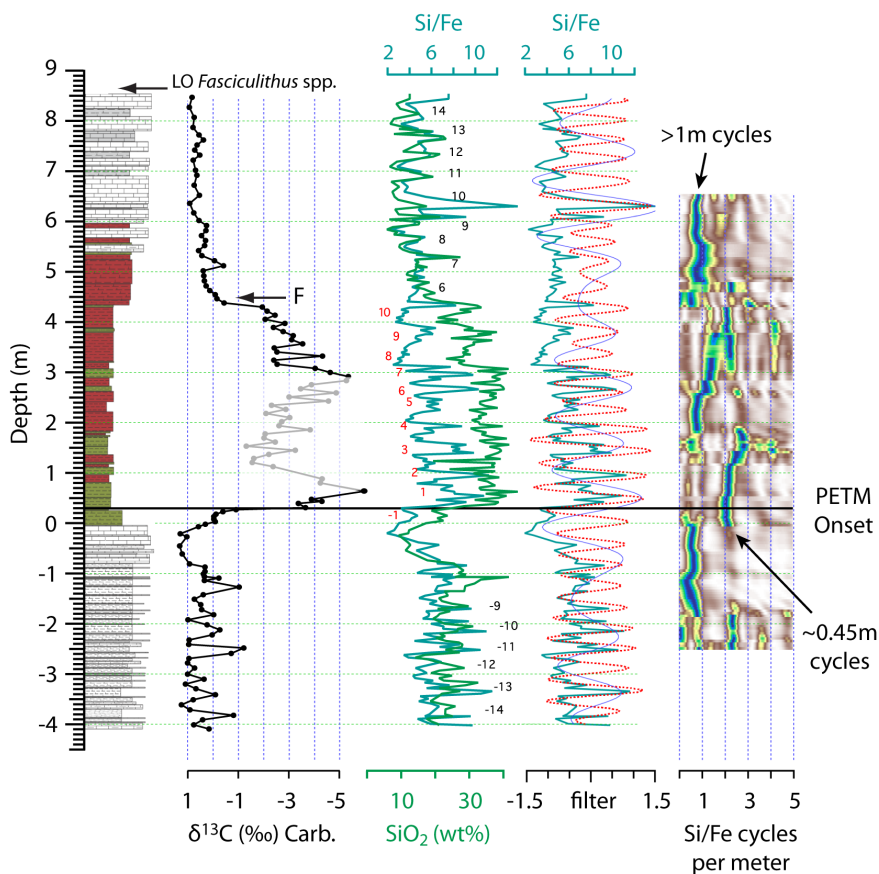
Figure 2. New sediment geochemistry data for the Zumaia section. From left to right: lithological log produced during sample collection for this study (2011); bulk carbonate δ¹³C; SiO₂ weight percent and Si/Fe ratio based on weight percents of oxides (SiO₂/Fe₂O₃) from bulk sediment XRF analyses, pre-PETM and post-PETM precession cycles numbered in black, intra-PETM half-precession cycles numbered in red; Si/Fe ratios with Gaussian filters of the dominant cycles 0.45m (red) and 1m (blue); evolutive spectral analysis for Si/Fe.
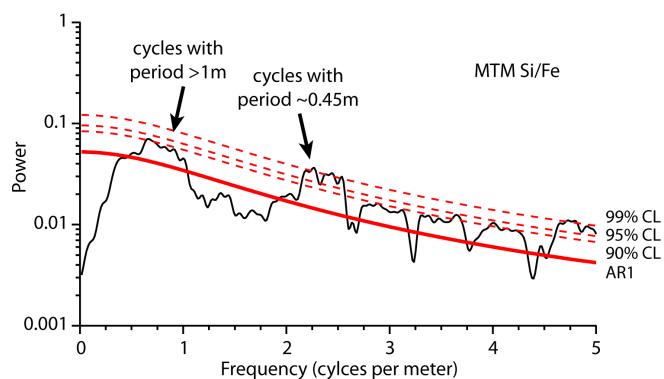
Figure 3. MTM power spectra for Si/Fe ratios; highlighted are spectral peaks equivalent to cycles with period >1 m and ~0.45 m.
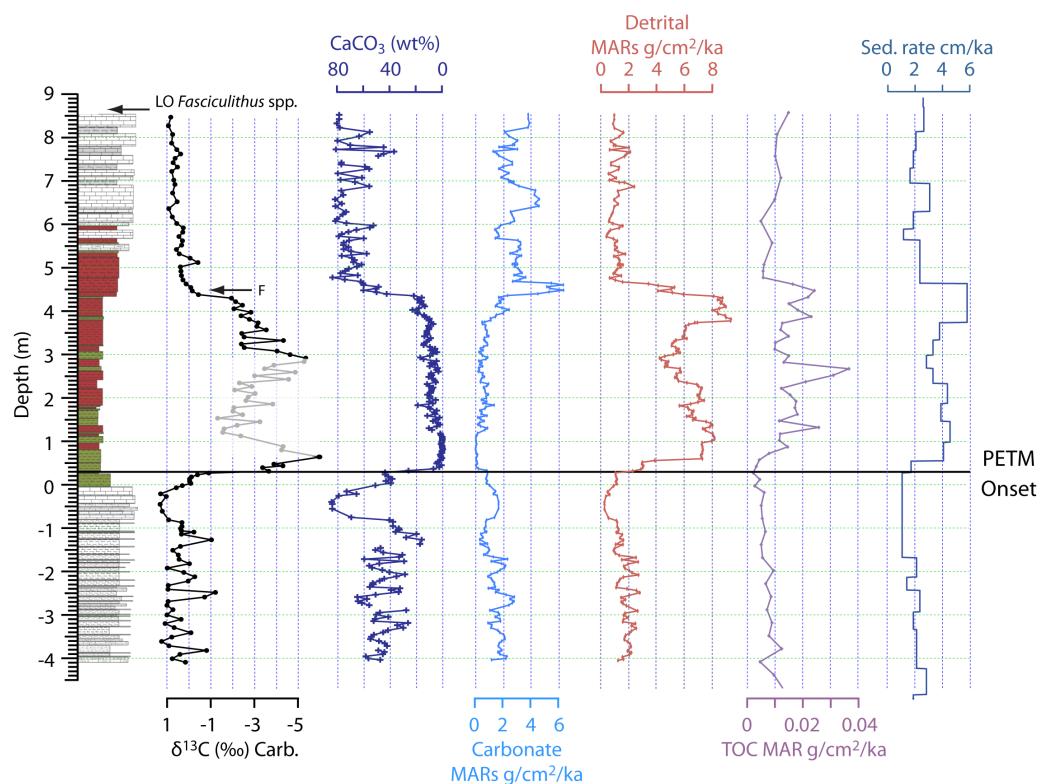
5

10

15

20

25

30

Climate of the Past

Open Access

Discussions

Figure 4. New carbonate, detrital and organic carbon mass accumulation and sedimentation rates for the Zumaia section. From left to right: lithological log produced during sample collection for this study (2011); bulk carbonate δ¹³C; weight percent CaCO₃ derived from XRF CaCO calibrated to discrete CaCO₃ analyses (see methods); CaCO₃ mass accumulation rate (light blue); detrital mass accumulation rate (red); organic carbon accumulation rate (purple); and, linear sedimentation rates (far right) derived from the new cyclostratigraphic framework.
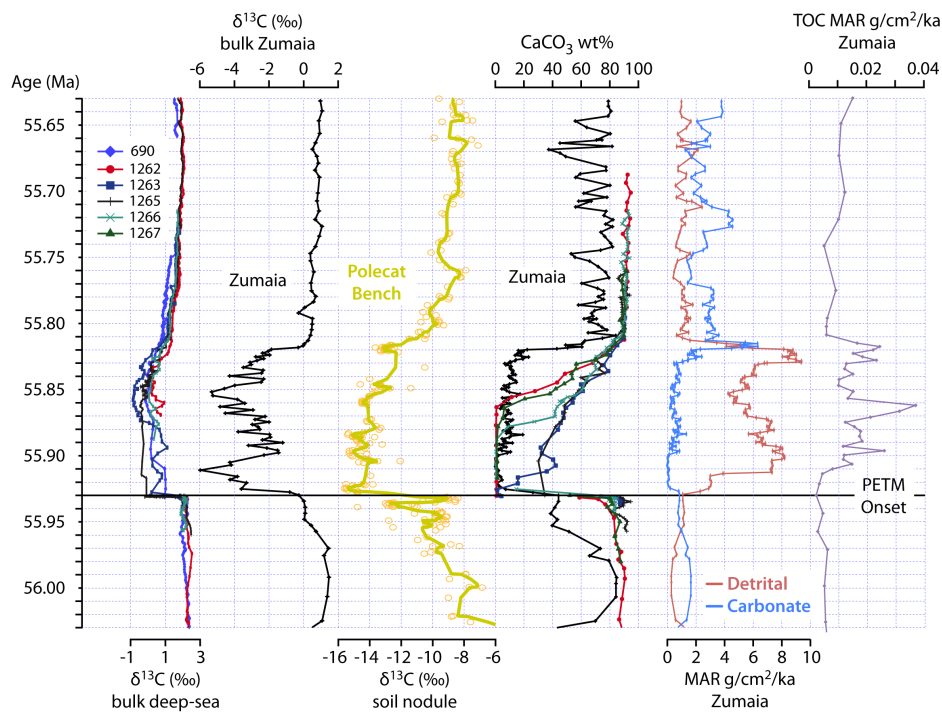
Figure 5. Comparison of the Zumaia records against terrestrial (Big Horn Basin) and deep-ocean sites (Walvis Ridge, ODP Sites 1262, 1263, 1265, 1266, 1267; Maud Rise ODP Site 690) on the same cyclostratigraphic age model. From left to right: bulk carbonate δ13C for deep ocean sites; bulk carbonate δ13C for Zumaia; soil nodule δ13C from the Big Horn Basin; CaCO3 records from Zumaia and the deep-ocean sites; detrital (red), CaCO3 (blue) and organic carbon (purple, far left) mass accumulation rates from Zumaia.

Climate
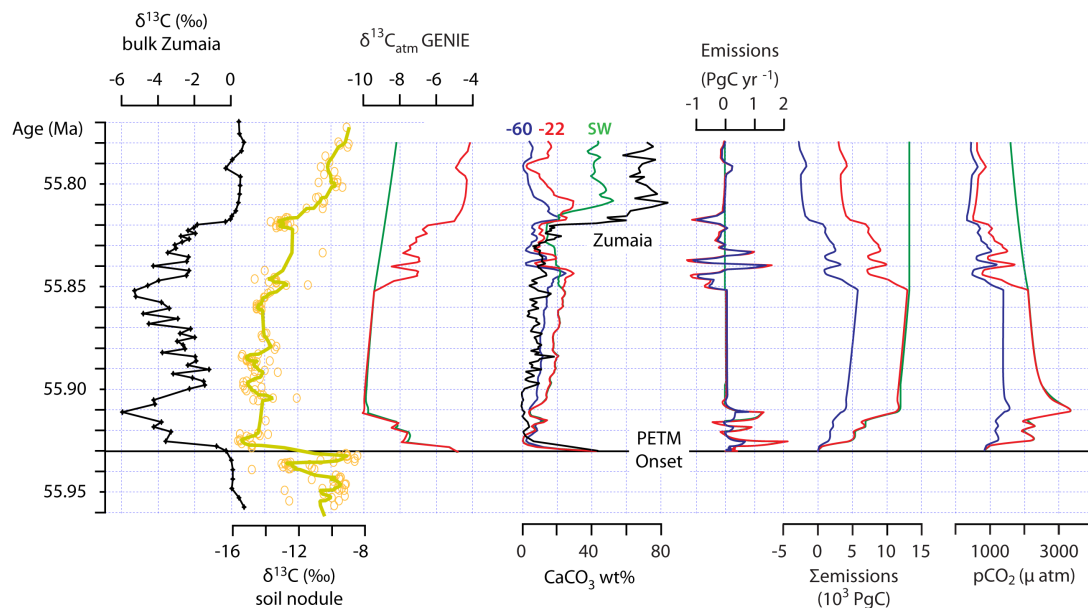of the Past

Discussions

Open Access

EGU

Figure 6. Results of inverse modelling with cGENIE Earth System Model. From left to right: the bulk carbonate δ¹³C for Zumaia which drives model inversions (black); soil nodule δ¹³C record of the Big Horn Basin (yellow), as representative of atmospheric CO₂ δ¹³C for comparison to model results; modelled δ¹³C composition of atmospheric carbon dioxide; carbon emission rate in PgC per year; cumulative carbon emissions (cumulative input minus removal); modelled atmospheric pCO₂; modelled and actual weight % CaCO₃ content of the sediment column at Zumaia; modelled carbon emission and removal rates; cumulative modelled carbon emissions / removal; modelled atmospheric pCO₂. The model scenarios are as follows: 1) carbon input at δ¹³C of -22 ‰ during the onset, no carbon removal (green); 2) carbon input and removal with δ¹³C of -22 ‰ to follow Zumaia target CIE (red); 3) carbon input with δ¹³C of -60 ‰ and removal of carbon with δ¹³C of -22 ‰ to follow Zumaia target CIE (blue). All simulations have active temperature-dependent silicate weathering feedbacks operative throughout.